Arch. Metall. Mater. **69** (2024), 3, 911-921

DOI: https://doi.org/10.24425/amm.2024.150911

H. TAZE[1], H. AHLATCI[1*], S. YAŞIN[1], D. ERGIN[1], Y. TÜREN[1], Z. ÖZEŞER[2], F. BIROL[2], S. TOZKOPARAN[2], T. ÇITRAK[2]

EFFECT OF ZINC AND SILICON ON TRIBOCORROSIVE WEAR BEHAVIORS OF HOT FORGED CuZn3Fe2Si3 AND CuZn15Si4 ALLOYS

The production and characterization of UNS C65620 (CuZn3Fe2Si3) and UNS C87800 (CuZn15Si4) coded alloys were investigated. The alloys poured into the gravity die casting method were hot forged with a ram, followed by stress relief annealing heat treatment. While the formation of Cu_4Si, $Cu_{0.83}Si_{0.17}$ and Cu_5Zn_8 phases were detected in the structure of the UNS C65620 coded alloy, $Cu_{12.75}SiZn_{2.92}$ and Cu_3Zn intermetallics with the phases given above were observed in the structure of the alloy containing more Zn and Si. The formation of phases containing more Si and Zn resulted in an increase in both the hardness and strength of the UNS C87800 coded alloy, while the decrease in the % reduction of area and the observation of dynamic deformation aging caused the increase in both the wear rate and deformation hardening rate, which led to embrittlement of the alloy. The deterioration of the corrosion resistance of the UNS C87800 coded alloy can be attributed to the formation of Zn-rich corrosion products on the surface during corrosion.

Keywords: Copper Alloys; Brass; Casting; Tribology; Corrosion

1. Introduction

Copper is one of the most prominent metals among the non-ferrous metals used by human beings in terms of its role in shaping civilizations. Its chemical, physical, and aesthetic properties create a wide range of usage in industry and high technology applications. Having the features of ease of manufacture, high electrical and thermal conductivity and forgeability, copper is also resistant to corrosion and wear [1-5]. The desire for high strength materials in engineering has led to the need to add a certain amount of some elements to pure copper [6]. Copper has a wide variety of alloying elements such as zinc, silicon, aluminum, iron, and nickel. By means of these elements, copper gains new characteristics for its usage in various applications [7]. Copper alloys, which are produced with the addition of zinc constitute an important alloy group. Especially the Cu-Zn-Si alloy group got priority for high strength, high toughness, good wear, and corrosion properties [8]. Zinc increases strength, hardness, and wear resistance in where silicon improves the tensile strength and mechanical properties. More focus has been placed on the industrial manufacture of Cu-Zn-Si alloys as research into these alloys advances. Cu-Zn-Si alloy materials used in aviation equipment, marine applications, and other fields include electrical pipes, valve bodies, connecting rods, fasteners, marine and mast line equipment, nuts, bolts, screws, rivets, nails, and wires [9]. In production, most metallic materials have undergone at least one deformation process such as rolling, forging, and extrusion. These processes do not only shape materials but also effectively reduce casting defects such as pores and slag inclusions [10, 11]. Therefore, it has been reported that the hot deformation process is generally used to improve grain size and eliminate casting defects that play an important role in improving the mechanical and tribological properties of these alloys [12]. It is well known that not only tribological factors are sufficient to express the basic properties of materials, but also working environments affect the performance of a material [13,14]. The working environment includes natural factors such as dry air, sea water, lubricant [15-17]. The aim of this study is to determinate the forgeability on the mechanical and corrosion properties of the high Si and Zn added UNS C87800 coded alloy and compared to that of the UNS C65620 coded wrought copper alloy in terms of the effect of zinc and silicon addition elements and environmental conditions such as 3.5 wt.% NaCl and 10 wt.% diluted boron oil solution.

[1] UNIVERSITY OF KARABUK, DEPARTMENT OF METALLURGICAL AND MATERIALS ENGINEERING, KARABUK, TURKEY
[2] SAĞLAM METAL INDUSTRY AND TRADE INC., KOCAELI, TURKEY

* Corresponding author: hahlatci@karabuk.edu.tr

2. Materials and methods

The UNS C65620 and UNS C87800 coded alloys were cast in Sağlam Metal Corporation (Gebze-Turkey). The alloys were prepared by melting them in a 5 M brand induction melting furnace at 1150°C under air atmosphere. The molten alloys were then poured into steel molds 50 mm in diameter and 200 mm in height, preheated to 250°C. Subsequently, both of the investigated alloys were annealed and forged at 650°C with a ram at a strain of 60% in multiple directions and then, the hot forged samples were subjected to stress relief annealing heat treatment at 260°C, for 2 hours. Heat treatment processes were carried out in the Protherm PLF Series 110-130 brand furnace. The chemical compositions of the investigated alloys are determined by XRF (X-ray fluorescence) analysis and given in TABLE 1.

The surfaces of the investigated alloys, which were prepared by standard metallographic procedures in the form of grinding (by 240-4000 grit SiC papers) and then polishing (by 0.3 μm alumina suspension) in the Microtest brand device, were etched with 5 g $FeCl_3$ + 16 ml HCl + 60 ml ethanol mixed etching solution for microstructural analysis. Microstructure images were obtained with Nikon Epiphot 200 brand optical microscope and Carl Zeiss Ultra Plus Gemini brand SEM device equipped with EDS (energy dispersive spectroscopy).

The XRD peaks of the $20 \times 20 \times 5$ mm^3 cut samples from the investigated alloys were detected with the Rigaku Ultima IV device at a scanning angle of 10°-90° and a scanning speed of 3°/min. The peaks, which were formed as a result of the XRD test were compared with the standard cards and thus, the phases in the structure were analyzed.

Vickers hardness test was applied by indentation the pyramid shaped tip indenter under 0.5 kg load for 15 seconds with SHIMADZU HMV 2T micro hardness device on the surfaces of the samples prepared by applying standard metallographic procedure. After the test, the hardness was evaluated by taking the average of the 5 measurements.

In order to determine the mechanical properties, tensile tests were carried out on the samples machined in ISO 6892-1 standard with the Zwick/Roell Z600 tensile device at 1.67×10^{-3} s^{-1} tensile rate and room temperature. The mechanical properties of each alloy were determined as the average of the tensile tests of at least 3 samples.

The surfaces, which were cut into cubes of $5 \times 5 \times 5$ mm^3 from the alloys examined were grinded with 1200 SiC sandpaper and then cleaned with pure water and ethanol in an ultrasonic device, respectively. The measurements of the surface areas and initial masses of the samples before dipping were determined with micrometer and 0.1 mg precision balance, respectively and then the samples were immersed in 3.5 wt.% NaCl solution. The immersed samples were taken from the corrosion solution at 2 hours intervals until 48 hours and the corrosive oxide layers on the surface were cleaned by keeping the samples in 100 ml sulfuric acid and 900 ml distilled water solution for 5 minutes and then evaluated by the mass loss. Immersion corrosion tests were performed 3 times for each alloy and the arithmetic mean of the results obtained was calculated. At the end of the test period, a detailed analysis was made by using SEM images, which were taken by Carl Zeiss Ultra Plus Gemini brand SEM analysis device, to determine the corrosion mechanisms of the corroded sample surfaces.

The samples prepared from the investigated alloys are molded with epoxy resin by soldering the back side of the samples with copper wire to transfer the current and front side of the sample surface was exposed to the corrosive media. An effective adhesive tape is adhered to the front surface of the samples to create 0.25 cm^2 of an atmosphere open circular surface. In the test cell (Isotherm Boro 3.3, 250 ml beaker), the test sample as the working electrode, the graphite rod acting as the counter electrode and the saturated calomel electrode (SCE) as the reference electrode were placed. In all of the experimental studies, without any current flowing through the system, the change of the open circuit potentials in mV between the working and reference electrodes was measured against time in 3.5 wt.% NaCl solution at room temperature. After reaching the equilibrium potential (*Ecorr*), the potentiodynamic polarization curves were created in the range of –0.25 V +0.25 V with respect to the open circuit potential, at a scanning speed of 1 mV.s^{-1} and recorded from the cathodic to the anodic direction. Corrosion potential (*Ecorr*) and corrosion current density (*Icorr*) were calculated from Tafel curves. For all parameters, the arithmetic mean of the results were obtained by performing 3 tests on the 'Gamry PC4/300 mA potentiostat/galvanostat Instruments' potentiodynamic polarization tester.

For the wear test, block on ring wear device was used, and the counter material was cylindrical 1.2379 cold work tool steel with a hardness of 55 HRC and a diameter of 54.6 mm. The investigated alloys prepared in $15 \times 15 \times 10$ mm^3 dimensions were worn out in dry conditions at 20, 40, 80 N loads and in corrosive environments (containing 3.5 wt.% NaCl and/or 10 wt.% diluted boron oil solution) under 80 N load on a surface area of 15×10 mm^2 at a speed of 0.02 ms^{-1}. Wear tests were carried out at 2000 meters intervals, in total 10000 meters of sliding distance. The wear behavior of the samples was evaluated by measuring the mass loss with 0.1 mg precision balance. A detailed analysis was carried out using SEM images, which were taken by Carl Zeiss Ultra Plus Gemini brand SEM analysis device, in order to determine the wear mechanisms of the alloys examined.

TABLE 1

Chemical composition of UNS C65620 and UNS C87800 coded alloys

Chemical Composition (wt.%)										
Material Code	**Cu**	**Zn**	**Pb**	**Sn**	**P**	**Mn**	**Fe**	**Ni**	**Si**	**Al**
UNS C65620	Balance	3.105	0.010	0.003	0.06	0.575	1.713	0.010	2.867	0.060
UNS C87800	Balance	15.51	0.002	0.004	0.07	0.005	0.124	0.017	4.159	0.002

3. Results and discussions

The optical microstructures of the UNS C65620 and UNS C87800 coded alloys are given in Fig. 1, respectively. In the microstructure images of the UNS C87800 coded alloy, annealing and mechanical twins (Fig. 1) within the grains were observed. Mechanical twins tend to be in the form of sharp-edged lenses that reduce long-range elastic stresses and are thought to occur during hot forging. Annealing twins were formed in the air-cooling stage after hot forging in the shape of straight sides [18,19]. Fig. 1 shows the spherical phases which are thought to be Cu_4Si within the geometrical drawing in the optical microstructure image of the UNS C65620 coded alloy. In Fig. 1, the white arrow in the optical microstructure image of the UNS C87800 coded alloy and the geometrical drawing shows the twinning regions.

As seen in Fig. 2, Cu_4Si, $Cu_{0.83}Si_{0.17}$ and Cu_5Zn_8 were formed in both alloys together with αCuZn solid solution. $Cu_{12.75}SiZn_{2.92}$ and Cu_3Zn intermetallics were observed in UNS C87800 coded alloy different from the UNS C65620 coded alloy. Nnakwo et al. [20] reported that Cu_3Si phase, which is intermetallic phase transition to α and α-β phase, formed in the microstructure analysis of Cu-3%Si bronze. In this study, contrary to the Cu_3Si phase, the formation of other Si-containing phases was observed to be compatible with the studies of Wang et al. [21] and also Güler and Özenbaş [22].

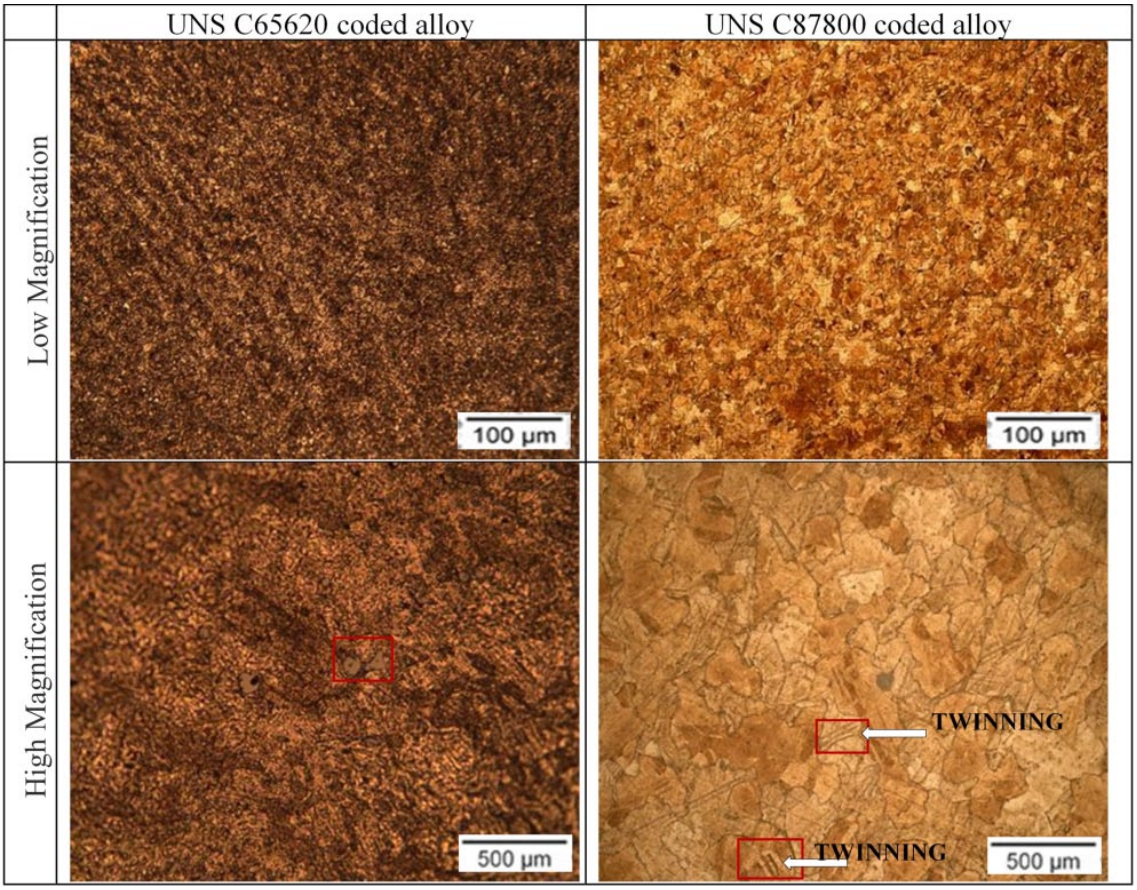

Fig. 1. The optical microstructure images of the hot forged and stress relief annealed UNS C65620 and UNS C87800 coded alloys

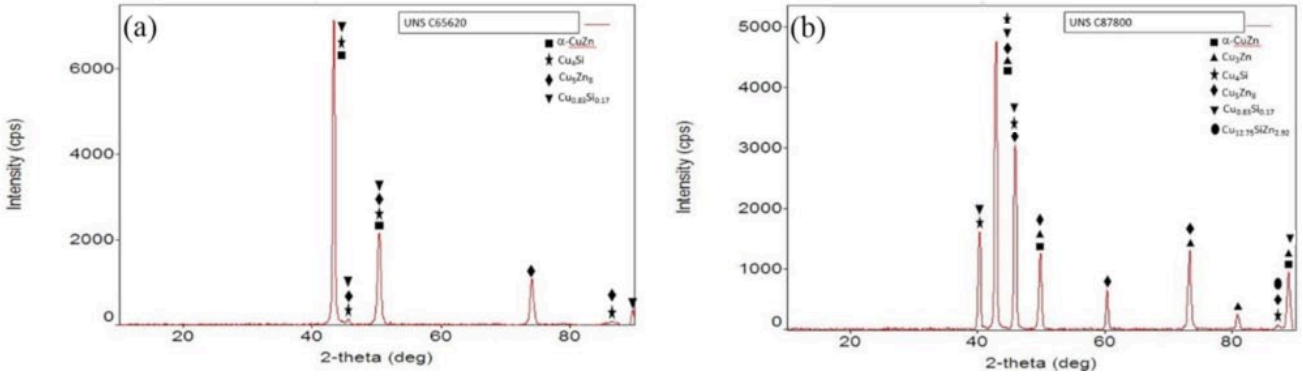

Fig. 2. The comparison of XRD analysis results of (a) UNS C65620 and (b) UNS C87800 coded alloys

SEM images and EDS analysis results of the investigated alloys are given in Fig. 3. In the SEM image of UNS C65620 coded alloy, EDS analysis of phase No.1 on the spherical gray colored mark and that of phase No. 2 shows Cu and Si-rich phases (Cu_4Si, $Cu_{0.83}Si_{0.17}$) and the matrix, respectively. Comparatively, in the microstructure of the UNS C87800 coded alloy the EDS results of No. 6, 7, 8 phases and that of No. 3, 4, 5 phases signs to belong to the gray colored Cu and Si-rich phases (Cu_4Si, $Cu_{0.83}Si_{0.17}$ and $Cu_{12.75}SiZn_{2.92}$) and the matrix, respectively. Chen et al. [23] observed that in the solidification of the $Cu_{70}Fe_{30}$ alloy, the iron-rich L2 phase is formed under equilibrium solidification conditions. The presence of iron was determined in the EDS analysis obtained from No. 1 area of the SEM image of the UNS C65620 coded alloy given in Fig. 3. Therefore, the formation of the phase particle, which includes Fe-containing Cu and Si together, can be observed in No. 1 area.

The hardness values of the alloys examined in this study are given in Fig. 4. The hardness of the UNS C87800 coded alloy led to a critical improvement by the increase in Zn and Si content, the formation of α-CuZn solid solution, the intermetallic (Cu_3Zn, Cu_5Zn_8, $Cu_{0.83}Si_{0.17}$ and $Cu_{12.75}SiZn_{2.92}$) phases and especially Cu_4Si phase. It was seen that the presence of high Cu content in the composition of the UNS C65620 coded alloy did not improve hardness. In accordance with this study, Savaşkan et al. [24] reported that increasing Cu content decreased hardness and tensile strength.

When the stress-strain curve of the investigated alloys given in Fig. 5 is examined, It is considered that the formation of saw-tooth shaped serrations originating from the high Si content of UNS C87800 coded alloy may be attributed to deformation aging. In the homogeneous plastic deformation region on the tensile test graph of the UNS C87800 coded alloy, the dissolved Si atoms significantly increased both the tensile strength and the % elongation up to the maximum tensile point, by leading to dynamic deformation aging, due to the inhibition of dislocation movements. Onodera et al. [25] investigated the presence or the absence of the Portevin-Le Chatelier effects in Cu-P, Cu-Ti, and Cu-Si alloys as functions of solute content. They reported that the serrated flows were observed at higher solute content and with less height of serration in the Si-bearing copper alloys than in the

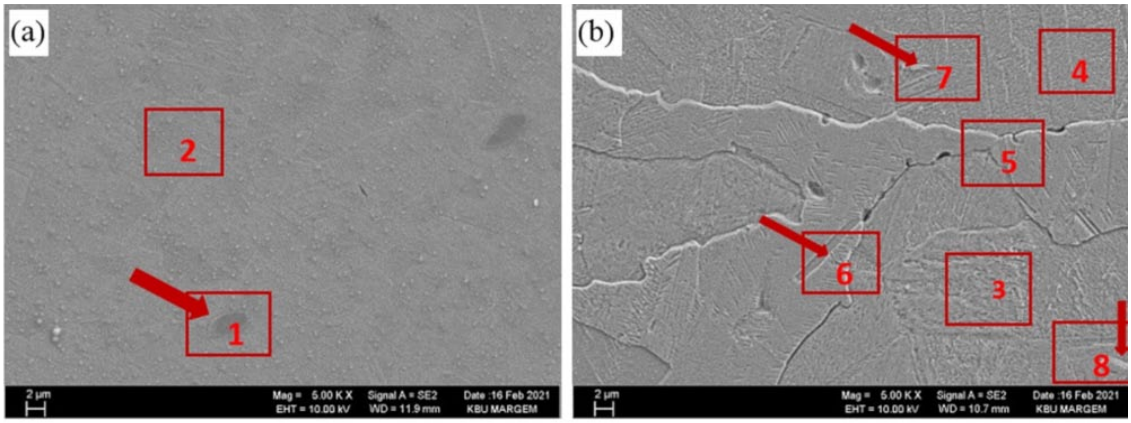

Mass percent (%)

Spectrum	Si	Fe	Cu	Zn
1	7.38	13.96	78.66	0.00
2	2.25	0.09	97.66	0.00

Mass percent (%)

Spectrum	Si	Fe	Cu	Zn
3	2.06	0.68	90.42	6.84
4	1.93	0.06	90.60	7.41
5	2.37	0.31	89.71	7.61
6	3.01	0.00	88.89	8.10
7	2.34	0.00	90.04	7.62
8	3.03	0.87	90.92	5.18

Fig. 3. SEM images and EDS analyzes of the (a) UNS C65620 and (b) UNS C87800 coded alloys

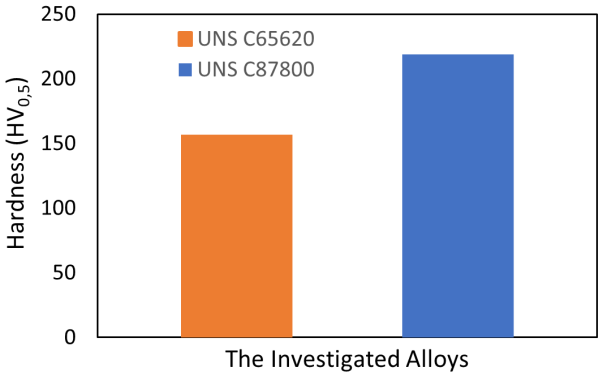

Fig. 4. The comparison of Vickers (HV) hardness test results of the UNS C65620 and UNS C87800 coded alloys

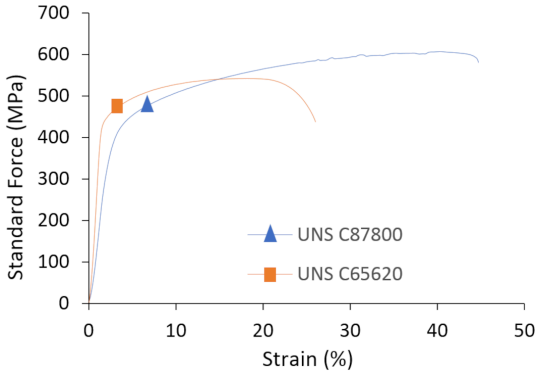

Fig. 5. The stress-strain curve of UNS C65620 and UNS C87800 coded alloys

P or Ti-bearing copper alloys. Therefore, the sawtooth behavior in the stress-strain curve obtained in this study was observed with less height. When the maximum tensile deformation point of the UNS C87800 codded alloy was reached, the material lost its % elongation capability, and this caused the fracture of the material exhibiting a lower % reduction of area compared to the UNS C65620 coded alloy after exceeding the maximum point.

In Fig. 6, according to the tensile test results of the UNS C65620 and UNS C87800 coded alloys, the difference between the yield and tensile strength of the UNS C87800 coded alloy is due to the work hardening ability. The strength of the UNS C65620 coded alloy was lower than that of the UNS C87800 coded alloy due to its low work hardening ability. However, an increase in % elongation observed in the UNS C87800 coded alloy can be attributed to the increase of both the strength and homogeneous plastic deformation zone by the observation of dynamic deformation aging. However, the lack of neck formation in the UNS C87800 coded alloy resulted in low % reduction of area. Although this is contrary to the traditional material behavior, the observation of dynamic deformation aging at room temperature of the UNS C87800 coded alloy improved the % elongation and decreased the % reduction of area. In the UNS C65620 coded alloy, the narrower homogeneous plastic deformation zone reduced the % elongation, but the extension of the non-homogeneous plastic deformation zone improved the % reduction of area after the maximum tensile point.

Nnakwo et al. [20] reported that the presence of dendritic primary silicon in the Cu-Zn-Si alloy system contributed to the low % elongation but moderately increase in tensile strength and hardness. In addition, the decrease in % elongation and the increase in hardness with the addition of Zn was attributed to the precipitation of the β-phase (Cu_4Si) in the alloy structure [20]. In this study, the factors affecting the mechanical properties of the UNS C65620 and UNS C87800 coded alloys can be shown as increase in hardness due to Zn content and dynamic deformation aging with the addition of Si content.

The relationship between the yield and tensile strength of the investigated alloys can be interpreted by the work hardening capacity (H_C) and rate (θ) parameters. These parameters can be calculated by Eq. (1) and Eq. (2), respectively.

$$H_C = \frac{\sigma_{UTS} - \sigma_{YS}}{\sigma_{YS}} = \frac{\sigma_{UTS}}{\sigma_{YS}} - 1 \tag{1}$$

$$\theta = \frac{d_\sigma}{d_\varepsilon} = \frac{\sigma_{UTS} - \sigma_{YS}}{\varepsilon_{UTS} - \varepsilon_{YS}} \tag{2}$$

Hereby, σ_{UTS} and σ_{YS} refer to ultimate tensile and yield stresses, ε_{UTS} and ε_{YS} refer to ultimate tensile and yield strains respectively (Eqs. (1) and (2)). TABLE 2 lists the deformation hardening capacity (H_C) and deformation hardening rate (Mpa) of the UNS C65620 and UNS C87800 coded alloys. The high deformation hardening capacity and deformation hardening rate of the UNS C87800 coded alloy led to both higher tensile strength and lower % reduction of area values.

TABLE 2

The comparison of deformation hardening capacity (H_C) and deformation hardening rate (MPa) of the UNS C65620 and UNS C87800 coded alloys

The Alloy Codes	Deformation Hardening Capacity (H_C)	Deformation Hardening Rate (Mpa)
UNS C65620	0.24	510.58
UNS C87800	0.70	669.87

In Fig. 7, SEM images of the fracture surfaces of the investigated alloys are given after the tensile test. The number of pits approximately the same in the fractography of investigated alloys. When compared to Fig. 7a, a large number of cavities appeared, with ridges along the edges, indicating an increase in the ductility of the UNS C87800 coded alloy (Fig. 7b). The increase in the deformation hardening rate of the UNS C87800 coded alloy (TABLE 2) indicates the plastic flow process.

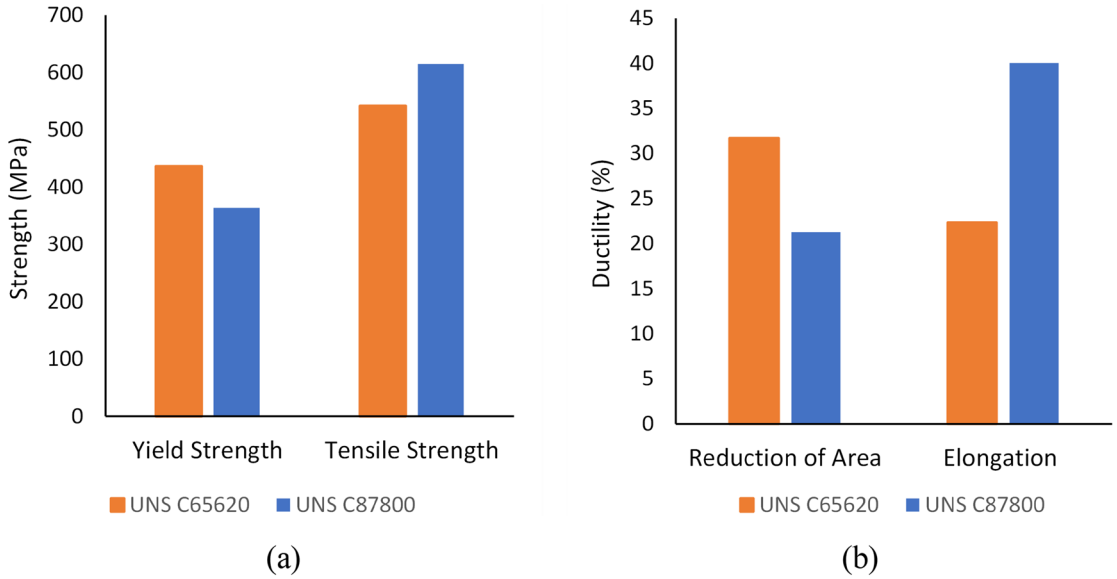

Fig. 6. The comparison of the (a) strength and (b) ductility results of the UNS C65620 and UNS C87800 coded alloys

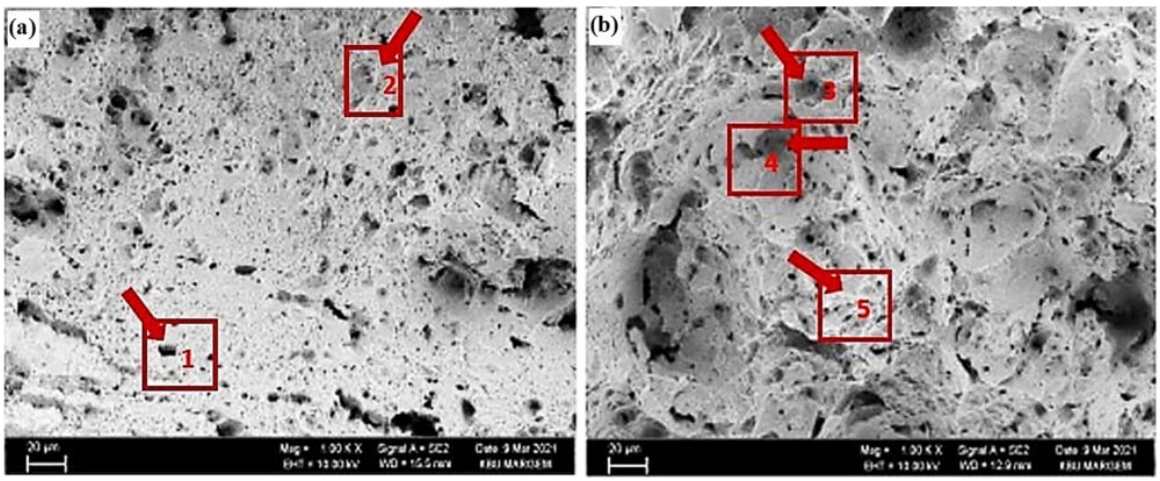

Fig. 7. The fracture surface SEM images of (a) UNS C65620 and (b) UNS C87800 coded alloys after the tensile test

Fig. 8a shows the mass loss (mg/dm^2) – time (h) relationship of the UNS C65620 and UNS C87800 coded alloys in 3.5 wt.% NaCl solution. UNS C87800 coded alloy exhibits the highest mass loss over a period of time. The variation in mass loss (mg/dm^2) were calculated by converting them to corrosion rate in unit of mdd (mg/(dm^2 × day)) and the graph of the variation against time (s) was drawn in Fig. 8b. As seen in Fig. 8b, the corrosion rate of the investigated alloys decreased until the 29th hour, reached the minimum value, and then increased again. The corrosion rate of the UNS C87800 coded alloy at 29th hour is higher than that of the UNS C65620 coded alloy.

Fig. 9 shows Tafel curves giving the Icorr (μA/cm^2) value versus the potential (V) change of the UNS C65620 and UNS C87800 coded alloys in 3.5 wt.% NaCl solution. Corrosion current density and corrosion potential values, which were obtained from the Tafel curves are given in TABLE 3. As seen in TABLE 3, when compared with the UNS C87800 coded alloy, the corrosion potential value (*Ecorr*) of the UNS C65620 coded alloy in the active direction and a slightly higher corrosion current density value can be explained as the low resistance to corrosion. This result contrasts with the results obtained by the immersion method. This can be attributed to the Zn and Si content found in the chemical composition of the UNS C87800 coded alloy. Potentiodynamic polarization test results performed by Singh et al. [26] and Basil et al. [27] supported the long-term immersion corrosion test results in this study. Singh et al. [26] and Basil et al. [27] found that corrosion resistance was high with a decrease in Si content. In accordance with these studies [26,27], it has been observed that the corrosion rate of the UNS C65620 coded alloy with low Si content was lower than that of the UNS C87800 coded alloy with high Si content according to the long immersion corrosion test results given in Fig. 8. This can be attributed to the denser (Fig. 2) formation of copper-silicide (Cu_4Si and $Cu_{0.83}Si_{0.17}$) in the structure of the UNS C65620 coded alloy. Contrary to this, the low corrosion current density and high corrosion potential values of the UNS C87800 coded alloy in the potentio-

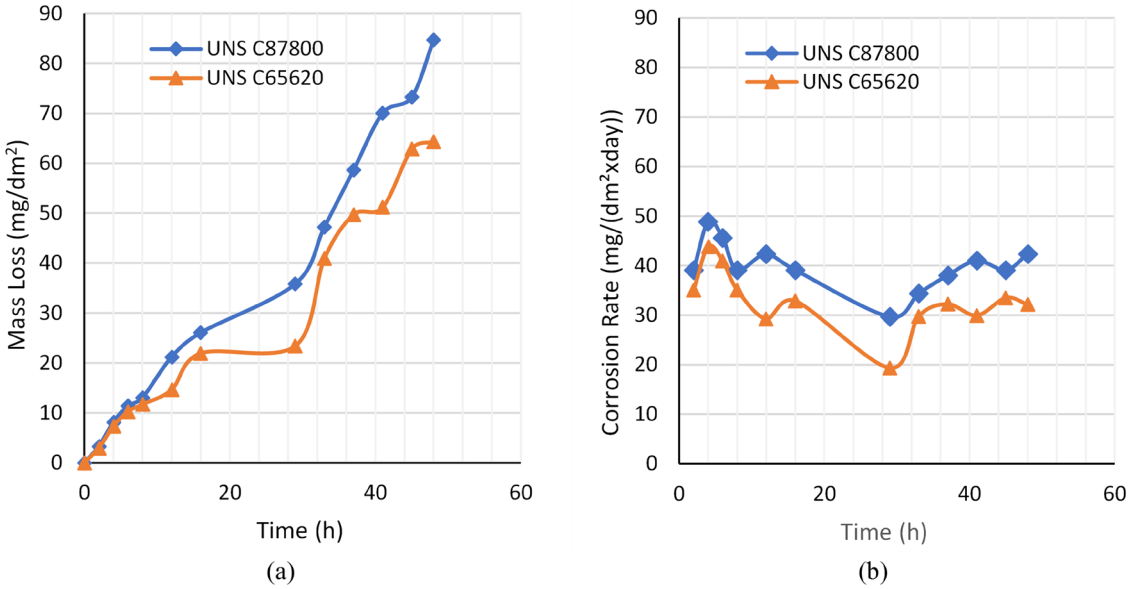

Fig. 8. The variation of (a) mass loss (mg/dm^2) and (b) corrosion rate (mg/(dm^2 × day)) for UNS C65620 and UNS C87800 coded alloys depending on time, after immersion test

dynamic polarization test results may be due to the presence of $Cu_{12.75}SiZn_{2.92}$ and Cu_3Zn phases formed in the microstructure.

TABLE 3

The comparison between *Icorr* (10^{-6} A/cm^2) and *Ecorr* (mV) results obtained from the Tafel curves of the UNS C65620 and UNS C87800 coded alloys

Material Code	*Icorr* (10^{-6} A/cm^2)	*Ecorr* (mV)
UNS C65620	6.74	-62.8667
UNS C87800	6.68	28.8

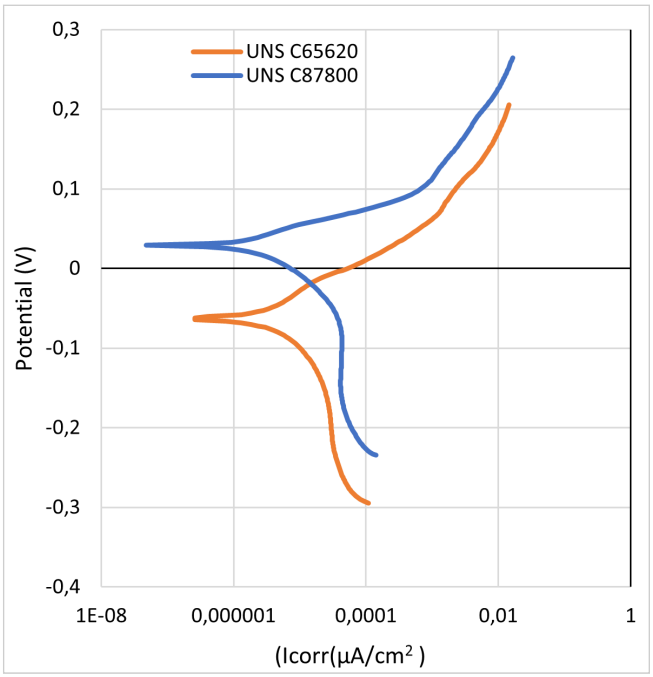

Fig. 9. Tafel curves of the UNS C65620 and UNS C87800 coded alloys after the potentiodynamic polarization tests

Fig. 10 shows the corrosion failure images of the investigated alloys after the immersion corrosion tests. The corrosion surfaces of the UNS C87800 coded alloy are deep rougher than that of the UNS C65620 coded alloy. Determination of averagely rich in Si content in EDS analysis results of the UNS C65620 coded alloy led to an improvement in the corrosion resistance of the alloy. The formation of Zn-rich areas into the deep marks on the corroded surface of the UNS C87800 alloy may explain the further corrosion damage after a long-term immersion corrosion test.

In Fig. 11, the sliding distance (m) – mass loss (g) relationships of the UNS C65620 and UNS C87800 coded alloys under 20, 40, 80 N in dry contact conditions and 80 N in corrosive environments (3.5 wt.% NaCl and 10 wt.% diluted boron oil solutions) are shown. The mass loss of the investigated alloys changes linearly depending on the sliding distance. The mass loss of the UNS C87800 coded alloy was higher than that of the UNS C65620 coded alloy at a certain sliding distance and all applied loads. Apart from the general tribological rules, it is seen that the mass loss is inversely proportional to the hardness and strength values such that the mass loss decreases as the hardness and strength of the alloys increase [28,29]. Although the UNS C87800 coded alloy has higher hardness, the UNS C65620 coded alloy showed better wear resistance. In accordance with this study, Savaşkan et al. [24] reported that mass loss decreased with increasing Cu content which reduced strength. The wear behaviors of the UNS C65620 and UNS C87800 coded alloys in corrosive environments was similar to that of the UNS C65620 and UNS C87800 coded alloys in dry contact conditions. Compared to the dry wear tests the mass loss decreased further with the change of the wear environment from 3.5 wt.% NaCl solution to 10 wt.% diluted boron oil solution compatible with Ref [30]. In some studies [30-33], particles detached from the sample worn surfaces increased the adhesion tendency and lubricating effect between counter materials and sample worn surface. The

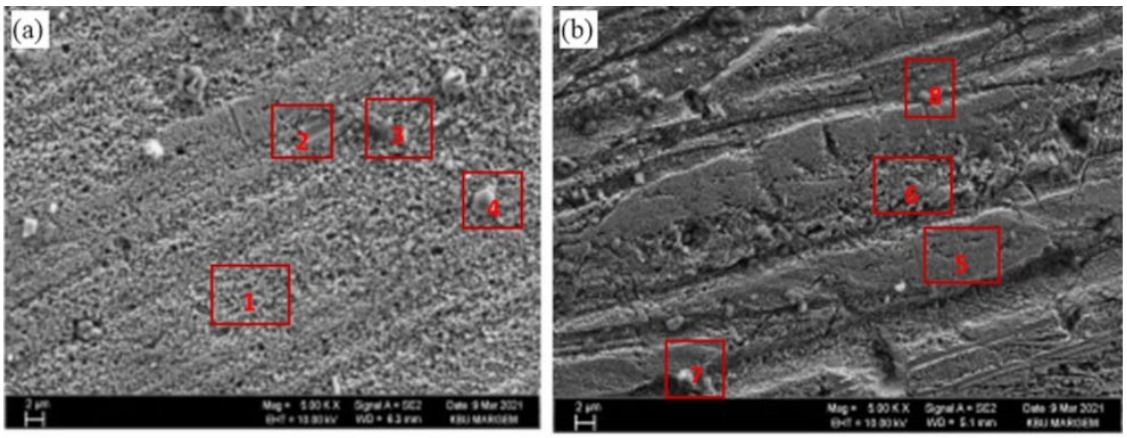

Mass percent (%)

Spectrum	Si	Fe	Cu	Zn
1	2.08	2.05	95.86	0.00
2	22.11	74.22	2.46	1.21
3	3.07	0.00	93.10	3.83
4	0.17	1.16	61.26	37.41

Mass percent (%)

Spectrum	Si	Cu	Zn
5	2.09	95.03	2.88
6	1.24	93.20	5.56
7	3.64	61.18	35.17
8	2.35	82.84	14.81

Fig. 10. The SEM images and EDS analyzes of the (a) UNS C65620 and (b) UNS C87800 coded alloys after the immersion corrosion test

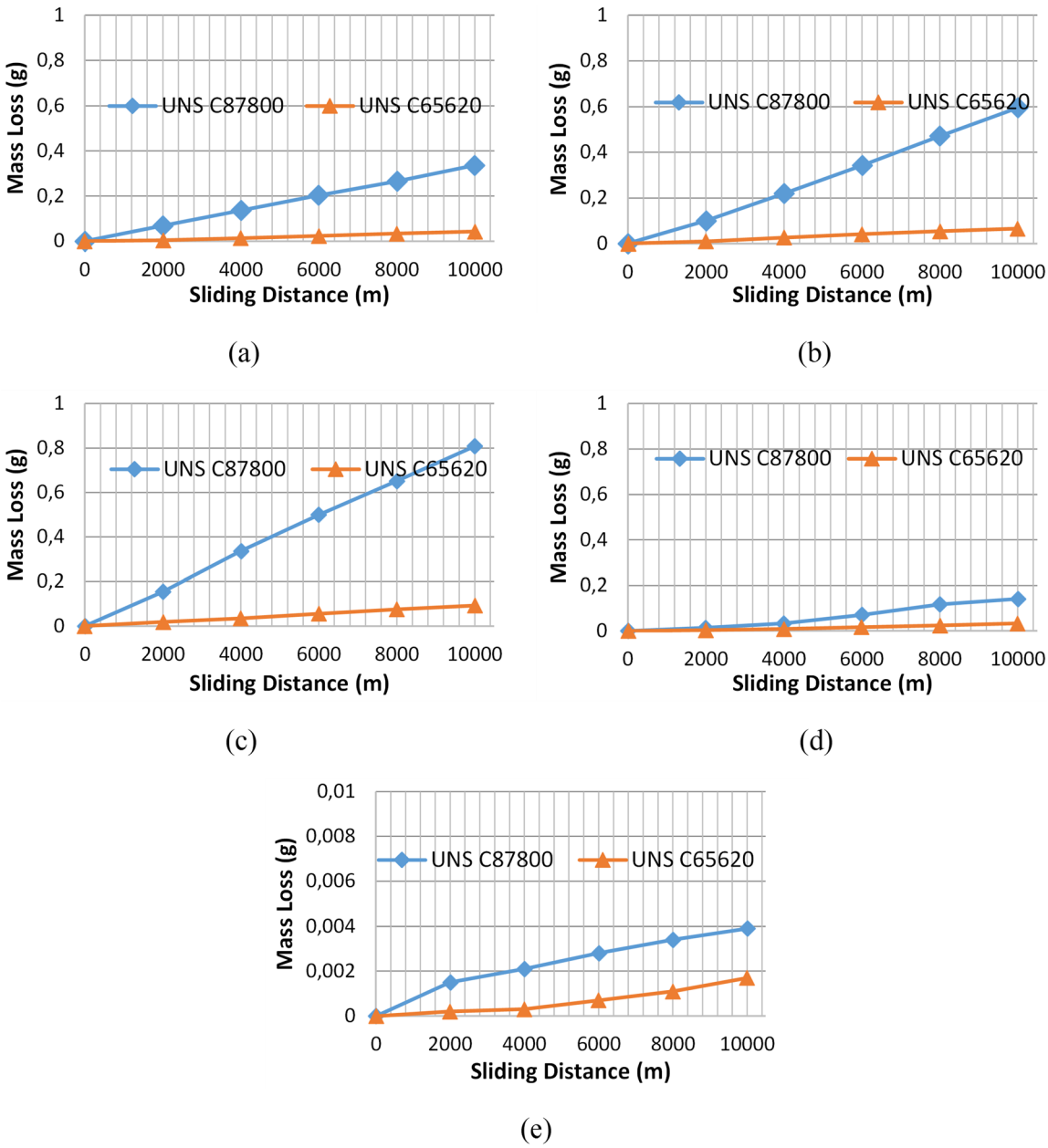

Fig. 11. The sliding distance (m) – mass loss (g) relationship of the UNS C65620 and UNS C87800 coded alloys under (a) 20 N, (b) 40 N, (c) 80 N in dry contact conditions, (d) 80 N in 3,5 wt.% NaCl solution, and (e) 80 N in 10 wt.% diluted boron oil solution

UNS C65620 coded alloy used in this study exhibited better wear resistance than the UNS C87800 coded alloy due to the lubricating properties of Cu, Fe and Si rich particles. Singh et al. [26] reported that the formation of copper-silicide had an effective on the high wear resistance.

In Fig. 12, SEM images of the worn surfaces of the UNS C65620 and UNS C87800 coded alloys after the wear test under 80 N in dry contact conditions and in corrosive environments (3.5 wt.% NaCl and 10 wt.% diluted boron oil solutions) are given. On the worn surface of the UNS C87800 coded alloy, abrasive sliding marks formed in the sliding direction, while the adhesive wear mechanism was observed in the UNS C65620 coded alloy, which was worn by plastering the debris by plastic deformation outside of the wear mark between the tested alloy and counter material surfaces. It led to improvement in the wear resistance of the alloy with the code UNS C65620 in accordance with Ref [29-35]. In UNS C87800 coded alloy, formation of the abrasive wear mechanism and embrittlement due to a decrease in the % reduction of area and increase in the deformation hardening rate expelled rupture debris out of the contact surface with the counter material; thus, resulting in further mass loss. Similar to the study of Birol and Isler [36] this situation can be explained by three-body abrasion leading to high material removal.

Although compared to the wear test in the dry contact conditions, similar wear mechanisms are observed in the corrosive environments (3.5 wt.% NaCl and 10 wt.% diluted boron oil solutions) a smooth geometric film was formed between the surfaces in 10 wt.% diluted boron oil solution. It has been observed to have a lubricating effect similar to the wear behavior in 3.5 wt.% NaCl solution [37].

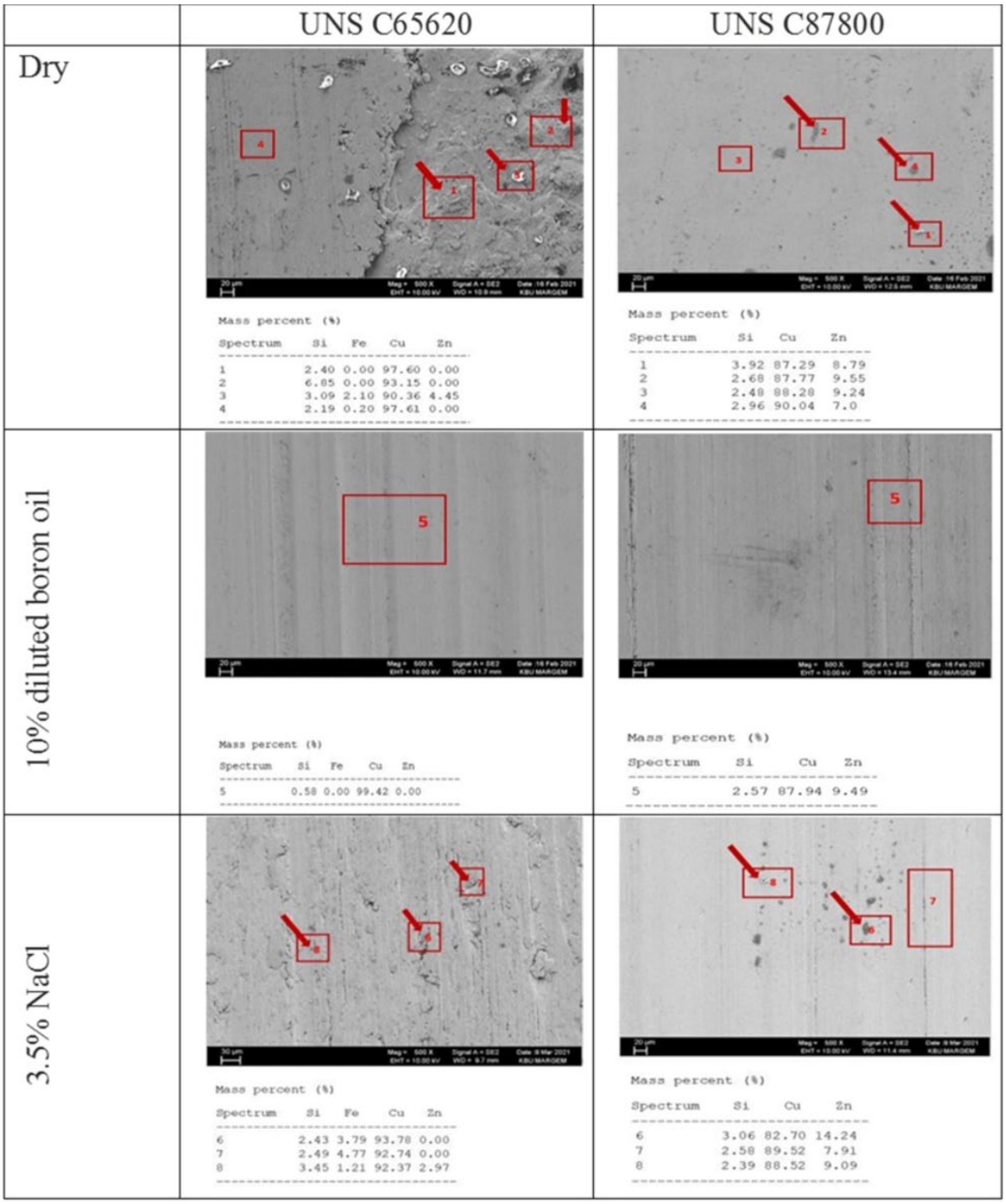

Fig. 12. SEM images and EDS analyzes of UNS C65620 and UNS C87800 coded alloys in dry environment, 10 wt.% diluted boron oil, and 3,5 wt.% NaCl solution after the wear test

4. Conclusions

The production and characterization of UNS C65620 and UNS C87800 coded alloys were examined. With the increase in Zn and Si content, the formation of α-CuZn solid solution and the other intermetallics (Cu_4Si, $Cu_{0.83}Si_{0.17}$ and $Cu_{12.75}SiZn_{2.92}$, Cu_3Zn, Cu_5Zn_8) phases led to an increase in the hardness and strength of the UNS C87800 coded alloy. The presence of α-CuZn matrix phase in the UNS C65620 coded alloy with high Cu content did not improve the hardness and strength. In the homogeneous plastic deformation region of the UNS C87800 coded alloy, the secondary phases (rich in Si and Zn) in the structure increase both the tensile strength and % elongation of UNS C87800 coded alloy up to the maximum point significantly by triggering dynamic deformation aging due to the inhibition of dislocation movements.

Increase in the corrosion rate of the UNS C87800 coded alloy was explained by the fact that the formation of Zn-rich areas (Cu_5Zn_8 and Cu_3Zn) in deep traces on the corroded surface after a long-time immersion corrosion test. It was observed that decrease in the corrosion rate of the UNS C65620 coded alloy with low Si content stemmed from the fact that copper-silicide

(Cu_4Si and $Cu_{0.83}Si_{0.17}$) phase formation. On the contrary, the low corrosion current density and high corrosion potential of the UNS C87800 coded alloy in the potentiodynamic polarization test results attributed to the presence of the phases ($Cu_{12.75}SiZn_{2.92}$ and Cu_3Zn) containing Zn.

While the observation of the adhesive wear mechanism on the worn surface of the UNS C65620 coded alloy with high Cu content improved the wear resistance, the formation of the abrasive wear mechanism of the UNS C87800 coded alloy with high Si and Zn content resulted in deterioration in the wear resistance. This is attributed to embrittlement of the UNS C87800 coded alloy by a decrease in the % reduction of area and increase in the deformation hardening rate. In addition, the wear resistance of the UNS C65620 coded alloy was due to the lubricating properties of the Fe and Si-rich particles in its content.

Acknowledgement

The authors acknowledge SAĞLAM METAL for their project IP No. 17, "Development of Cu-Zn-Si Alloys of which Corrosion and Abrasion Resistance Increased by Heat Treatment: Alternative to Aluminum Bronzes Used in Aviation, Maritime and Defense Industries", TÜBİTAK for the project No. 1649B022010972 and Karabük University for the BAP project No. KBÜBAP-21-YL033.

REFERENCES

[1] S.G. Shabestari, H. Moemeni, Effect of copper and solidification conditions on the microstructure and mechanical properties of Al–Si–Mg alloys. Journal of Materials Processing Technology **153**, 193-198 (2004). DOI: https://doi.org/10.1016/j.jmatprotec.2004.04.302

[2] D.E. Tyler, W.T. Black, Introduction to Copper and Copper Alloys. In: ASM Handbook Committee (Ed.), Properties and Selection: Nonferrous Alloys and Special-Purpose Materials, ASM International (1990). DOI: https://doi.org/10.31399/asm.hb.v02.a0001065

[3] H. Chandler, Metallurgy for the Non-metallurgist. ASM International 1998.

[4] A. Tuthill, Guidelines for the use of copper alloys in seawater. Materials Performance **26**, 12-22 (1987).

[5] J.A. Rogers, Dispersion-strengthened copper alloys with useful electrical and mechanical properties. Powder Metallurgy **20** (4), 212-220 (1977). DOI: https://doi.org/10.1179/pom.1977.20.4.212

[6] P. García, S. Rivera, M. Palacios, J. Belzunce, Comparative study of the parameters influencing the machinability of leaded brasses. Engineering Failure Analysis **17** (4), 771-776 (2010). DOI: https://doi.org/10.1016/j.engfailanal.2009.08.012

[7] Z. Weiwen, X. Wei, W. Li-ping, W. Yuanbiao, P. Guoru, Mechanical properties and tribological behavior of a cast heat-resisting copper based alloy. J. Cent. South Univ. Technol. **9** (4), 235-239 (2002). DOI: https://doi.org/10.1007/s11771-002-0034-y

[8] I.K.G. Sugita, R. Soekrisno, I.M.M. Suyitno, Mechanical and damping properties of silicon bronze alloys for music applications. Int. J. Eng. & Technol. **11** (6), 98-105 (2011)

[9] M. Kulczyk, J. Skiba, S. Przybysz, W. Pachla, P. Bazarnik, M. Lewandowska, High strength silicon bronze (C65500) obtained by hydrostatic extrusion. Archives of Metallurgy and Materials **57**, 859-862 (2012). DOI: https://doi.org/10.2478/v10172-012-0094-4

[10] W.R. Cribb, M.J. Gedeon, F.C. Grensing, Performance advances in copper-nickel-tin spinodal alloys. Advanced Materials & Processes **171** (9), 20-26 (2013).

[11] Y. Jiang, Z. Li, Z. Xiao, Y. Xing, Y. Zhang, M. Fang, Microstructure and properties of a Cu-Ni-Sn alloy treated by two-stage thermomechanical processing. JOM. **71** (8), 2734-2741 (2019). DOI: https://doi.org/10.1007/s11837-019-03606-5

[12] C. Zhao, Z. Wang, D. Li, D. Pan, B. Lou, Z. Luo, W. Zhang, Optimization of strength and ductility in an as-extruded Cu–15Ni–8Sn alloy by the additions of Si and Ti. Journal of Alloys and Compounds **823**, 153759 (2020). DOI: https://doi.org/10.1016/j.jallcom.2020.153759

[13] D.M. Liu, Q.S. Wang, W. Yuan, X.J. Mi, A Comparative study on the friction and wear properties of three different copper alloys. Materials Science Forum **913**, 205-211 (2018). DOI: https://doi.org/10.4028/www.scientific.net/msf.913.205

[14] M. Okayasu, D. Izuka, Y. Ninomiya, Y. Manabe, T. Shiraishi, Mechanical and wear properties of Cu-Al-Ni-Fe-Sn-based alloy. Advances in materials Research **2** (4), 221-235 (2013). DOI: https://doi.org/10.12989/amr.2013.2.4.221

[15] M. Chen, X.H. Shi, H. Yang, P.K. Liaw, M.C. Gao, J.A. Hawk, J. Qiao, Wear behavior of $Al_{0.6}CoCrFeNi$ high-entropy alloys: Effect of environments. Journal of Materials Research **33**, 3310-3320 (2018). DOI: https://doi.org/10.1557/jmr.2018.279

[16] S. Baskar, G. Sriram, Tribological Behavior of Journal Bearing Material under Different Lubricants. Tribology in Industry **36** (2), 127-133 (2014)

[17] M. Yasar, M. Demiral, D. Ozyurek, M. Unal, Investigation of wear behaviors of C95200-C95300 CuAl-Fe alloys. Industrial Lubrication and Tribology **61** (1), 40-46 (2009). DOI: https://doi.org/10.1108/00368790910929520

[18] H.Y. Wu, F.J. Zhu, S.C. Wang, W.R. Wang, C.C. Wang, C.H. Chiu, Hot deformation characteristics and strain-dependent constitutive analysis of Inconel 600 superalloy. Journal of Materials Science **47**, 3971-3981 (2012). DOI: https://doi.org/10.1007/s10853-012-6250-4

[19] S. Mahajan, C.S. Pande, M.A. Imam, B.B. Rath, Formation of annealing twins in fcc crystals. Acta Mater. **45** (6), 2633-2638 (1997). DOI: https://doi.org/10.1016/S1359-6454(96)00336-9

[20] K.C. Nnakwo, I.U. Okeke, E.E. Nnuka, Effect of zinc content on the structure and mechanical properties of silicon bronze. Int. J. Sci. Res. Sci. Eng. Technol. **3**, 179-183 (2017).

[21] J. Wang, H. Xu, S. Shang, L. Zhang, Y. Du, W. Zhang, S. Liu, P. Wang, Z.-K. Liu, Experimental investigation and thermodynamic modeling of the Cu–Si–Zn system with the refined description for the Cu–Zn system. Calphad **35**, 191-203 (2011). DOI: https://doi.org/10.1016/j.calphad.2011.02.001

[22] M. Özenbaş, H. Güler, Formation of Al-Si intermetallic phases. Chemical Engineering Communications **190** (5-8), 911-924 (2003). DOI: https://doi.org/10.1080/00986440302126

[23] Y.Z. Chen, F. Liu, G.C. Yang, X.Q. Xu, Y.H. Zhou, Rapid solidification of bulk undercooled hypoperitectic Fe–Cu alloy. Journal of alloys and compounds **427**, L1-L5 (2007). DOI: https://doi.org/10.1016/j.jallcom.2006.03.012

[24] T. Savaşkan, A.P. Hekimoğlu, G. Pürçek, Effect of copper content on the mechanical and sliding wear properties of monotectoid-based zinc-aluminium-copper alloys. Tribology International **37** (1), 45-50 (2004). DOI: https://doi.org/10.1016/S0301-679X(03)00113-0

[25] R. Onodera, T. Ishibashi, H. Era, M. Shimizu, The portevin-le chatelier effects in Cu-Ti, Cu-P and Cu-Si alloys. Acta Metallurgica **32** (5), 817-822 (1984). DOI: https://doi.org/10.1016/0001-6160(84)90155-X

[26] I. Singh, D.K. Basu, M.N. Singh, A.K. Bhattamishra, S.C. Dev, Role of silicon in the corrosion resistance of Cu-Si alloys in natural seawater. Anti-Corrosion Methods and Materials **44** (3), 195-199 (1997). DOI: https://doi.org/10.1108/00035599710167160

[27] D.K. Basil, A.K. Bhattamishra, S.C. Dev, I. Singh, Studies on corrosion behaviour of Cu-Si alloys in Sulphide and Chloride media. Anti-Corrosion Methods and Materials **42** (5), 14-16 (1995). DOI: https://doi.org/10.1108/eb007368

[28] K.H. Zum Gahr, Microstructure and wear of materials. Elsevier, 1987.

[29] S. Kaiser, M.S. Kaiser, Wear Behavior of Commercial Pure Copper with Al and Zn under Dry, Wet and Corrosive Environment. Journal of Materials and Environmental Sciences **11** (4), 551-563 (2020).

[30] M.S. Kaiser, S.H. Sabbir, M.S. Kabir, M.R. Soummo, M.A. Nur, Study of mechanical and wear behaviour of hyper-eutectic Al-Si automotive alloy through Fe, Ni and Cr addition. Materials Research **21**, 1-9 (2018). DOI: http://dx.doi.org/10.1590/1980-5373-MR-2017-1096

[31] J.P. Tu, M.S. Liu, Wet abrasive wear of ordered Fe_3Al alloys. Wear **209** (1-2), 31-36 (1997). DOI: https://doi.org/10.1016/S0043-1648(97)00016-1

[32] S. Wirojanupatump, P.H. Shipway, A direct comparison of wet and dry abrasion behaviour of mild steel. Wear **233**, 655-665 (1999). DOI: https://doi.org/10.1016/S0043-1648(99)00208-2

[33] https://www.aircraftmaterials.com/data/copper/ams4616.html Accessed 11 Nov 2021

[34] K. Elleuch, R. Elleuch, R. Mnif, V. Fridrici, P. Kapsa, Sliding wear transition for the CW614 brass alloy. Tribology International **39** (4), 290-296 (2006). DOI: https://doi.org/10.1016/j.triboint.2005.01.036

[35] J.P. Tu, Y.Z. Yang, L.Y. Wang, X.C. Ma, X.B. Zhang, Tribological properties of carbon-nanotube-reinforced copper composites. Tribology Letters **10** (4), 225-228 (2001). DOI: https://doi.org/10.1023/A:1016662114589

[36] Y. Birol, D. Isler, Abrasive wear performance of AlCrN-coated hot work tool steel at elevated temperatures under three-body regime. Wear **270** (3-4), 281-286 (2011). DOI: https://doi.org/10.1016/j.wear.2010.10.069

[37] H. Kasem, O. Stav, P. Grützmacher, C. Gachot, Effect of low depth surface texturing on friction reduction in lubricated sliding contact. Lubricants **6**, 62 (2018). DOI: https://doi.org/10.3390/lubricants6030062